Efficient finite-difference time-domain scheme for light scattering by dielectric particles: application to aerosols

Ping Yang, K. N. Liou, Michael I. Mishchenko, and Bo-Cai Gao

We have examined the Maxwell-Garnett, inverted Maxwell-Garnett, and Bruggeman rules for evaluation of the mean permittivity involving partially empty cells at particle surface in conjunction with the finite-difference time-domain (FDTD) computation. Sensitivity studies show that the inverted Maxwell-Garnett rule is the most effective in reducing the staircasing effect. The discontinuity of permittivity at the interface of free space and the particle medium can be minimized by use of an effective permittivity at the cell edges determined by the average of the permittivity values associated with adjacent cells. The efficiency of the FDTD computational program is further improved by use of a perfectly matched layer absorbing boundary condition and the appropriate coding technique. The accuracy of the FDTD method is assessed on the basis of a comparison of the FDTD and the Mie calculations for ice spheres. This program is then applied to light scattering by convex and concave aerosol particles. Comparisons of the scattering phase function for these types of aerosol with those for spheres and spheroids show substantial differences in backscattering directions. Finally, we illustrate that the FDTD method is robust and flexible in computing the scattering properties of particles with complex morphological configurations.

OCIS codes: 010.1290, 010.1310, 010.3920, 290.5850, 290.1090, 280.1100.

1. Introduction

The finite-difference-time domain (FDTD) technique is one of the most promising methods for solution of the scattering properties of nonspherical and inhomogeneous particles.[1–3] The fundamental principle of this method has remained essentially unchanged since its inception more than 30 years ago,[1] that is, the electromagnetic field is solved on a discrete lattice on the basis of time-dependent Maxwell equations. In the FDTD computation the spatial domain must be discretized by use of a grid mesh. It is well known that a Cartesian grid is more practical and flexible than a curvilinear or target-conforming grid mesh because the latter type of grid mesh is usually applicable only to some specific geometries. In addition, a non-Cartesian difference scheme may substantially complicate the criterion of computational stability, boundary conditions, and the specification of the radiation source. When a particle with a curved surface is defined over a Cartesian grid, its geometry is approximately represented by a number of cubic cells in a staircasing manner. The staircasing effect can potentially be large if the dielectric constants of the particle differ substantially from those of the host medium. To reduce this effect in the FDTD computation, Yang and Liou[2,3] applied the Maxwell-Garnett rule[4] to evaluate the mean permittivity of the partially empty cells at the particle surface where subgrid variations of the optical constants exist. However, various methods can be used to compute the mean permittivity, and their relative performance requires further study.

In addition to the staircasing effect, a discontinuity of permittivity exists at a cell edge located at the interface of a particle medium and free space, even if the grid mesh is target conforming (e.g., the Cartesian grid for a cubic geometry), a fact that had not been addressed in the FDTD implementation. In

When this research was performed, P. Yang and K. N. Liou were with the Department of Atmospheric Sciences, University of California, Los Angeles, Los Angeles, California 90095. P. Yang (pyang@climate.gsfc.nasa.gov) is now with Science Systems and Applications, Incorporated, Lanham, Maryland 20706. M. I. Mishchenko is with the NASA Goddard Institute for Space Studies, New York, New York 10025. B.-C. Gao is with the Remote Sensing Division, U.S. Naval Research Laboratory, Washington, D.C. 20375.

Received 21 October 1999; revised manuscript received 24 April 2000.

0003-6935/00/213727-11$15.00/0

the time-marching iterations for computing the near field, permittivity values at cell edges are required. Thus an appropriate averaging procedure must be used to overcome the discontinuity of permittivity at a cell edge if the optical constants for the four adjacent cells are different. In this study we have improved the Cartesian FDTD scheme by minimizing the staircasing effect and the discontinuity of permittivity at the interface of the particle medium and free space. Because the performance of the absorbing boundary is critical to the accuracy of the FDTD solution, we also applied the newly developed perfectly matched layer (PML) absorbing boundary condition.[5,6] In Section 2 we present three approaches to evaluating the mean dielectric constants for a given grid cell and suggest an appropriate way to compute effective dielectric constants at cell edges. To apply the PML technique we developed an equivalent version of Berenger's PML equations.[6] In Section 2 the program-coding technique is discussed in terms of reduction of CPU time and memory requirements. Section 3 describes the numerical tests that we carried out to investigate the relative performance of various approaches to determining the mean and effective dielectric constants for grid cells and cell edges. Applications to light scattering by nonspherical aerosols are described in Section 4. Conclusions are given in Section 5.

2. Cartesian Finite-Difference Time-Domain Scheme

A. Mean Permittivity for Partially Empty Cells

When a nonrectangular particle is defined in a Cartesian grid mesh, grid cells located near the particle surface may be partially empty. Because subgrid features cannot be specified in the Cartesian discrete lattice, a brute-force approach is usually used for determining the dielectric constants for these surface cells; that is, a cell is considered to be empty (with unity permittivity) if half of the cell volume is outside the particle. Otherwise, the dielectric properties of the particle are assigned to the cell. This approach produces a sharp truncation in terms of dielectric properties in representing the scattering particle by a step-by-step approximation, and the pertinent staircasing effect may be potentially large. Thus it is necessary to evaluate the mean dielectric constant for the partially empty cells.

The Maxwell-Garnett[4] and Bruggeman[7] rules have commonly been applied to the evaluation of the mean dielectric constant associated with inhomogeneity. For a given volume containing two dielectric media (host and inclusion), the mean dielectric constant given by the Maxwell-Garnett rule is

$$\bar{\varepsilon} = \varepsilon_m \left[\frac{\varepsilon + 2\varepsilon_m + 2f(\varepsilon + 2\varepsilon_m)}{\varepsilon + 2\varepsilon_m - f(\varepsilon + 2\varepsilon_m)} \right], \tag{1}$$

where ε_m and ε are the permittivities of the host and the inclusion media, respectively, and f is the volume fraction of the inclusion. It can be seen that the roles of host and inclusion in Eq. (1) are not reciprocal. If we transpose the roles of the two media in the Maxwell-Garnett rule, we obtain the inverted Maxwell-Garnett rule as follows:

$$\bar{\varepsilon} = \varepsilon \left[\frac{\varepsilon_m + 2\varepsilon + 2(1-f)(\varepsilon_m + 2\varepsilon)}{\varepsilon_m + 2\varepsilon - (1-f)(\varepsilon_m + 2\varepsilon)} \right]. \tag{2}$$

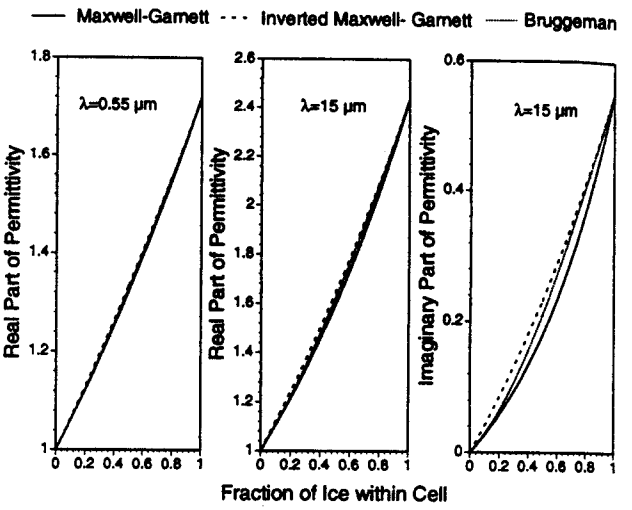

Fig. 1. Mean permittivity evaluated from Maxwell-Garnett, inverted Maxwell-Garnett, and Bruggeman rules for grid cells composed of free space and ice at 0.55 and 15 μm. The refractive indices for the two wavelengths are, respectively, $1.311 + i3.11 \times 10^{-9}$ and $1.571 + i0.1756$.

The Bruggeman rule can be expressed in the following general form:

$$\frac{1}{\Delta v} \int\int\int_{\Delta v} \frac{\varepsilon(\vec{r}) - \bar{\varepsilon}}{\varepsilon(\vec{r}) + 2\bar{\varepsilon}} \, dv = 0, \tag{3}$$

where Δv is the spatial region for accounting for the inhomogeneity of dielectric properties. If only two media are considered, Eq. (3) reduces to

$$f \frac{\varepsilon - \bar{\varepsilon}}{\varepsilon + 2\bar{\varepsilon}} + (1-f) \frac{\varepsilon_m - \bar{\varepsilon}}{\varepsilon_m + 2\bar{\varepsilon}} = 0. \tag{4}$$

Note that the roles of the host and inclusion media are reciprocal in the Bruggeman equation. Equation (4) is nonlinear and complex, and its solution is not straightforward. For practical calculations, we have derived an efficient iterative scheme for the solution of Eq. (4), given by

$$\bar{\varepsilon}_{n+1} = \frac{\varepsilon\varepsilon_m + 2[f\varepsilon + (1-f)\varepsilon_m]\bar{\varepsilon}_n}{f\varepsilon_m + (1-f)\varepsilon + 2\bar{\varepsilon}_n}. \tag{5}$$

With an initial value of $\bar{\varepsilon}_0 = f\varepsilon + (1-f)\varepsilon_m$, a convergent solution can be obtained with iterations in fewer than ten steps.

Figure 1 shows the mean permittivity values evaluated from Eqs. (1), (2), and (4) for a cell composed of free space and ice at 0.55- and 15-μm wavelengths. The refractive indices of ice for these two wavelengths are $1.311 + i3.11 \times 10^{-9}$ and $1.571 + i0.1756$, respectively. Note that the complex per-

mittivity ($\varepsilon_r + i\varepsilon_i$) is related to the complex refractive index ($m_r + im_i$) as follows:

$$\varepsilon_r = m_r^2 - m_i^2, \qquad \varepsilon_i = 2m_r m_i. \tag{6}$$

From Fig. 1 it is evident that the differences in permittivity evaluated from the three schemes are very small for the optically thin case at 0.55 μm. Because the absorption of ice at 0.55 μm is extremely small, it does not make a noticeable difference in the evaluation of the mean imaginary part of the permittivity. For the 15-μm wavelength, however, the imaginary part of the refractive index is quite large. In this case, the absorption properties computed from the FDTD technique depend on the approach used to evaluate the mean permittivity. The mean permittivity evaluated by the Bruggeman rule lies between those evaluated from the Maxwell-Garnett and inverted Maxwell-Garnett rules. Results computed from Bruggeman's equation converge to those determined from Maxwell-Garnett's equation if the cells are nearly empty, and they converge to the values evaluated from the inverted Maxwell-Garnett rule when ice dominates the cells. However, the overall patterns of variation of mean permittivity versus fraction of host medium are similar for the three approaches.

B. Effective Permittivity at Cell Edges

The finite-difference analog of Maxwell's equations has a staggered form; that is, the electric field is evaluated at the cell edges at time step n, whereas the magnetic field is evaluated at the center of cell faces at time step $n + 1/2$. Thus, for time-marching iterative computation of the electric field, the permittivity values at the cell edges must be known. It is straightforward to specify the permittivity value at a cell edge if the four adjacent cells have the same dielectric properties. However, there is a discontinuity or singularity of permittivity at the cell edge if the four adjacent cells are heterogeneous. In this case it is neither mathematically suitable nor physically correct to assume indiscriminately that the value of the permittivity at the cell edge is the value associated with one of the adjacent cells, although this approach has commonly been employed for numerical realization of the FDTD technique. To derive an appropriate value of permittivity at the cell edge we begin with the discretization of Maxwell's equations. Consider the z component of the E field as an example. The equation that governs the temporal variation of an electric field is given by

$$\frac{\varepsilon_r(\vec{r})}{c}\frac{\partial \hat{E}(\vec{r}, t)}{\partial t} + k\varepsilon_i(\vec{r})\hat{E}(\vec{r}, t) = \nabla \times \hat{H}(\vec{r}, t), \tag{7}$$

where c is the speed of light in vacuum, $k = \omega/c$, where ω is the angular frequency of the electromagnetic wave, and the real and imaginary parts of permittivity can be computed from Eqs. (6). Let the cell center be denoted $(x, y, z) = (I\Delta x, J\Delta y, K\Delta z)$, where Δx, Δy, and Δz are the cell dimensions along the three coordinate axes. Integration of the z component of the expression in Eq. (7) over the domain enclosed by the dotted lines shown in Fig. 2 leads to

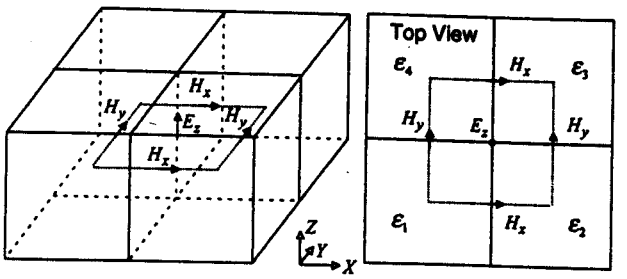

Fig. 2. Geometry for a cell edge and four adjacent cells in a Cartesian grid.

$$\int_{I\Delta x}^{(I+1)\Delta x}\int_{J\Delta y}^{(J+1)\Delta y} [\nabla \times \hat{H}(\vec{r}, t)]_z dxdy$$
$$= \Delta x\{H_x[\vec{r}(I + 1/2, J, K), t] - H_x[\vec{r}(I + 1/2, J + 1, K), t]\} + \Delta y\{H_y[\vec{r}(I + 1, J + 1/2, K), t] - H_y[\vec{r}(I, J + 1/2, K), t]\}, \tag{8}$$

where $\vec{r}(I + 1/2, J, K)$ represents the position vector for point $[(I + 1/2)\Delta x, J\Delta y, k\Delta z]$. It should be pointed out that the discretization in Eq. (8) does not produce any truncation error. Furthermore, integrating the left-hand side of Eq. (7) yields

$$\int_{I\Delta x}^{(I+1)\Delta x}\int_{J\Delta y}^{(J+1)\Delta y}\left[\frac{\varepsilon_r(\vec{r})}{c}\frac{\partial E_z(\vec{r}, t)}{\partial t} + k\varepsilon_i(\vec{r})E_z(\vec{r}, t)\right]dxdy$$
$$= \left[\frac{\bar{\varepsilon}_r(I + 1/2, J + 1/2, K)}{c}\frac{\partial}{\partial t} + k\bar{\varepsilon}_i(I + 1/2, J + 1/2, K)\right]\int_{I\Delta x}^{(I+1)\Delta x}\int_{J\Delta y}^{(J+1)\Delta y} E_z(\vec{r}, t)dxdy$$
$$\approx \left[\frac{\bar{\varepsilon}_r(I + 1/2, J + 1/2, K)}{c}\frac{\partial}{\partial t} + k\bar{\varepsilon}_i(I + 1/2, J + 1/2, K)\right]E_z[\vec{r}(I + 1/2, J + 1/2, K), t]\Delta x\Delta y, \tag{9}$$

where $\bar{\varepsilon}_r(I + 1/2, J + 1/2, K)$ and $\bar{\varepsilon}_i(I + 1/2, J + 1/2, K)$ are the effective permittivities evaluated at the cell edge. From Eq. (8) and relation (9) we obtain the following difference-differential equation:

$$\frac{\bar{\varepsilon}_r[\vec{r}(I + 1/2, J + 1/2, K)]}{c}\frac{\partial E_z[\vec{r}(I + 1/2, J + 1/2, K), t]}{\partial t} + k\bar{\varepsilon}_i[\vec{r}(I + 1/2, J + 1/2, K)]E_z[\vec{r}(I + 1/2, J + 1/2, K), t]$$
$$= \{H_x[\vec{r}(I + 1/2, J, K), t] - H_x[\vec{r}(I + 1/2, J + 1, K), t]\}/\Delta y + \{H_y[\vec{r}(I + 1, J + 1/2, K), t] - H_x[\vec{r}(I, J + 1/2, K), t]\}/\Delta x. \tag{10}$$

The temporal derivative in Eq. (10) can be discretized in a straightforward manner by use of either a leap-frog or an exponential scheme. Note that the discretization in time will not affect the effective permittivity at the cell edge because it is a time-independent variable. To evaluate the effective permittivity we let the complex permittivity values for the four adjacent cells be $\varepsilon_1 = \varepsilon_{r1} + i\varepsilon_{i1}$, $\varepsilon_2 = \varepsilon_{r2} + i\varepsilon_{i2}$, $\varepsilon_3 = \varepsilon_{r3} + i\varepsilon_{i3}$, and $\varepsilon_4 = \varepsilon_{r4} + i\varepsilon_{i4}$. It follows that

$$\bar{\varepsilon}_r(I+1/2, J+1/2, K) = \left[\varepsilon_{r1}\int_{I\Delta x}^{(I+1/2)\Delta x}\int_{J\Delta y}^{(J+1/2)\Delta y} + \varepsilon_{r2}\int_{(I+1/2)\Delta x}^{(I+1)\Delta x}\int_{J\Delta y}^{(J+1/2)\Delta y} + \varepsilon_{r3}\int_{(I+1/2)\Delta x}^{(I+1)\Delta x}\int_{(J+1/2)\Delta y}^{(J+1)\Delta y} + \varepsilon_{r4}\int_{I\Delta x}^{(I+1/2)\Delta x}\int_{(J+1/2)\Delta y}^{(J+1)\Delta y}\right] E_z(\vec{r}, t)\mathrm{d}x\mathrm{d}y \Big/ \int_{I\Delta x}^{(I+1)\Delta x}\int_{J\Delta y}^{(J+1)\Delta y} E_z(\vec{r}, t)\mathrm{d}x\mathrm{d}y \approx (\varepsilon_{r1} + \varepsilon_{r2} + \varepsilon_{r3} + \varepsilon_{r4})/4. \quad (11)$$

The error for the approximation in relation (11) is small because the tangential component of the electric field is continuous across the interface, as required by the electromagnetic boundary condition. Similarly, we have

$$\bar{\varepsilon}_i(I+1/2, J+1/2, K) \approx (\varepsilon_{i1} + \varepsilon_{i2} + \varepsilon_{i3} + \varepsilon_{i4})/4. \quad (12)$$

The preceding procedure of averaging the cell permittivity is mandatory for any particle geometry defined in a Cartesian grid, even if the staircasing approximation for defining the particle geometry is absent. For example, a cubic particle can be well defined in the Cartesian grid without the staircasing approximation. However, the cell edges at the particle surface are surrounded by both empty cells and dielectric medium cells, a condition for which, to avoid discontinuity, an average of the permittivity is required.

C. Perfectly Matched Layer Absorbing Boundary Condition

The performance of the absorbing boundary condition is critical to the accuracy of the FDTD technique. Various analytical absorbing boundary equations have been developed in the past two decades (see Ref. 8 and the papers cited therein). These boundary equations usually require a substantial white space between the boundary and the scattering target, thereby reducing the efficiency of the FDTD method in terms of CPU and memory requirements. Berenger's PML[5,6] has been widely applied to various FDTD implementations. Numerical experiments have shown that the spurious reflection associated with the PML boundary condition is approximately 3 orders of magnitude less than that produced by an analytical boundary equation.[9] The PML technique has been successfully applied to light scattering by ice crystals.[10] Yang and Liou[11] have shown that the absorption of the PML boundary condition is fundamentally due to the introduction of artificial diffusions in Maxwell's equations. For a systematic presentation of this study, here we recapitulate the PML boundary equations expressed in a format that contains diffusion terms.

The diffusions are imposed on the electromagnetic field components that are parallel to the boundary. In practice, the field must to be separated into two components, one parallel and one perpendicular to the boundary, that is,

$$(E_x, E_y, E_z) = [(E_{xy} + E_{xz}), (E_{yx} + E_{yz}), (E_{zx} + E_{zy})], \quad (13a)$$

$$(H_x, H_y, H_z) = [(H_{xy} + H_{xz}), (H_{yx} + H_{yz}), (H_{zx} + H_{zy})], \quad (13b)$$

The PML equations for the E_x and H_x components, for example, are

$$\frac{\exp[-\tau_y(y)t]}{c}\frac{\partial}{\partial t}\{\exp[\tau_y(y)t]E_{xy}\} = \frac{\partial(H_{zx} + H_{zy})}{\partial y}, \quad (14a)$$

$$\frac{\exp[-\tau_z(z)t]}{c}\frac{\partial}{\partial t}\{\exp[\tau_z(z)t]E_{xz}\} = -\frac{\partial(H_{yx} + H_{yz})}{\partial z}, \quad (14b)$$

$$\frac{\exp[-\tau_y(y)t]}{c}\frac{\partial}{\partial t}\{\exp[\tau_y(y)t]H_{xy}\} = -\frac{\partial(E_{zx} + E_{zy})}{\partial y}, \quad (14c)$$

$$\frac{\exp[-\tau_z(z)t]}{c}\frac{\partial}{\partial t}\{\exp[\tau_z(z)t]H_{xz}\} = \frac{\partial(E_{yx} + E_{yz})}{\partial z}, \quad (14d)$$

where $\tau_y(y)$ and $\tau_z(z)$ are zero, except in the boundary layers perpendicular to the y and z axes. The present form for the PML boundary equations is equivalent to that given by Berenger.[6] In practical computations, the diffusion parameters $\tau_y(y)$ and $\tau_z(z)$ can be specified from zero at the interface of free space and the artificial diffusion medium to their maximum values at the outermost layer. For example, $\tau_y(y)$ can be defined as

$$\tau_y(y) = \tau_{y,\max}[(y - y_0)/D]^p, \quad (15)$$

where $(y - y_0)$ is the distance of a grid point from the interface of free space and the PML medium, $D = L\Delta y$ is the thickness of the artificial diffusion medium for the boundary perpendicular to the y axis, and p is usually selected to be in the range 2–3. The param-

eter $\tau_{y,\max}$ can be specified in terms of the reflectance of the boundary for normal incidence as follows:

$$\tau_{y,\max} = -\frac{p+1}{2D}\ln[R(0°)]c, \tag{16}$$

where $R(0°)$ is the boundary reflection factor for normal incidence. The mean absorption must be taken into account for each cell distance in discrete computations. Thus the following two mean values for the electric and the magnetic fields can be used:

$$\bar{\tau}_y(J) = \frac{1}{\Delta y}\int_{J-1/2\Delta x}^{(J+1/2)\Delta x} \tau_y(y)\mathrm{d}y = \frac{\tau_{y,\max}}{p+1}\frac{(J+1/2)^{p+1} - (J-1/2)^{p+1}}{L^{P+1}} \quad E \text{ field}, \tag{17a}$$

$$\bar{\tau}_y(J+1/2) = \frac{1}{\Delta y}\int_{J\Delta y}^{(J+1)\Delta y} \tau_y(y)\mathrm{d}y = \frac{\tau_{y,\max}}{p+1}\frac{(J+1)^{p+1} - J^{p+1}}{L^{P+1}} \quad H \text{ field}. \tag{17b}$$

In this study we use the PML absorbing boundary condition with seven layers of artificial diffusion medium that are separated from the scattering target by eight layers of white space. According to the sensitivity study of Lazzi and Gandi,[12] we select $p = 2.5$ and $R(0°) = 5 \times 10^{-6}$.

D. Program Coding Improvement

Advances in the FDTD algorithms coupled with the increasing power of computers now make it possible to apply this method to size parameters up to 20 on an ordinary workstation. For particles with refractive index close to unity, FDTD computation has been carried out on a supercomputer for size parameters up to 40.[10] The grid size can be much larger in an optically thin case than in an optically thick case. The huge CPU and memory requirements of the FDTD technique are still a major concern in practical applications. However, a substantial reduction in computer resources can be achieved by proper program coding.

During the course of computational experimentation we found that the efficiency of the FDTD technique can be greatly improved if the computational program is coded in FORTRAN90 rather than in FORTRAN77. In particular, the array-oriented feature in FORTRAN90 can substantially reduce the CPU time for initialization and updating of the huge arrays involved in the time-marching iterations of the near field and in the Fourier-transform calculations that yield the field values in the frequency domain. In addition, FORTRAN90 permits dynamic storage allocation. With this feature the temporal working arrays that specify particle constants and the PML coefficients can be deallocated immediately as long as they are not required for further computation. The efficiency of the FDTD computational program can also be improved by use of various intrinsic functions that are permitted in FORTRAN90. Yang and Liou[3] have formulated an algorithm to map the near field (in the frequency domain) to the corresponding far field on the basis of a volume integral of the electric field inside the scattering particle. With the dynamic memory allocation feature of FORTRAN90, three one-dimensional arrays can be allocated with the exact array sizes in the computations to handle the three Cartesian components of the E field with only nonempty cells. Moreover, the FDTD computation can be largely vectorized with these one-dimensional arrays in the Fourier-transform procedure for the field values in the frequency domain and in mapping the near file to the far field.

3. Numerical Tests and Discussions

We have improved the FDTD program for light scattering by dielectric particles developed by Yang and Liou[3] by updating the absorbing boundary condition with the PML technique as well as by coding the program in FORTRAN90. For a size parameter of 10, the CPU requirement is reduced by a factor of 2 and the memory requirement is decreased by approximately 10%. The improvement is more substantial for larger-sized parameters. With the improved program, we conducted sensitivity computations in conjunction with the various schemes for evaluating mean and effective permittivities. Because the FDTD technique does not give preferential treatment to any specific particle shape (with the exception of rectangular targets in a Cartesian grid), a canonical study based on spheres can be a representative test of the technique's performance. For this reason, the present computations focus on the scattering properties of ice spheres at the 15-μm infrared wavelength at which the refractive index differs substantially from unity. A spherical particle defined in a Cartesian grid lattice is a pseudosphere with step-by-step surface roughness. The magnitude of the surface roughness or staircasing effect is proportional to the grid cell size and inversely proportional to the particle dimension. It follows that the present sensitivity study focuses on two representative cases with size parameters of 1 and 10.

Figure 3 shows a comparison of the phase functions of ice spheres computed from Mie theory and from the FDTD technique for a size parameter of 1. In the latter technique we applied the Maxwell-Garnett, inverted Maxwell-Garnett, and Bruggeman rules to evaluate the mean permittivity for the cells near the particle surface. In addition, we used an average of the permittivity given by relations (11) and (12) to define the effective permittivity at cell edges if the adjacent cells are different in dielectric constants. Three grid sizes, $\Delta s = \lambda/20$, $\lambda/25$, $\lambda/30$, were selected, where λ is the wavelength in vacuum and Δs ($=\Delta x = \Delta y = \Delta z$) is the grid cell size. From Fig. 3 it can be seen that the inverted Maxwell-Garnett rule performs best of the three approaches to evaluating

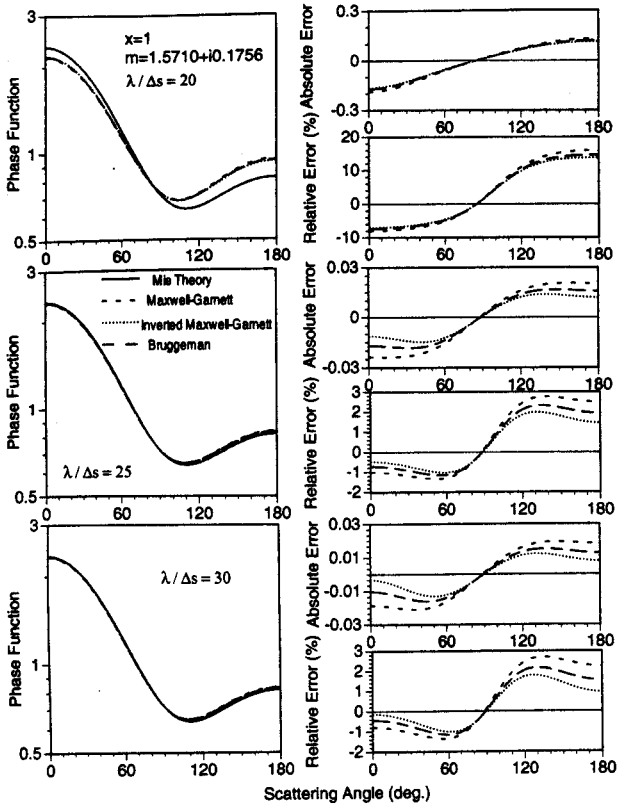

Fig. 3. Comparison of FDTD and Mie results for the phase functions of ice spheres at 15 μm for a size parameter of 1. Three approaches are used for evaluating the mean permittivity for partially empty cells located near the particle surface.

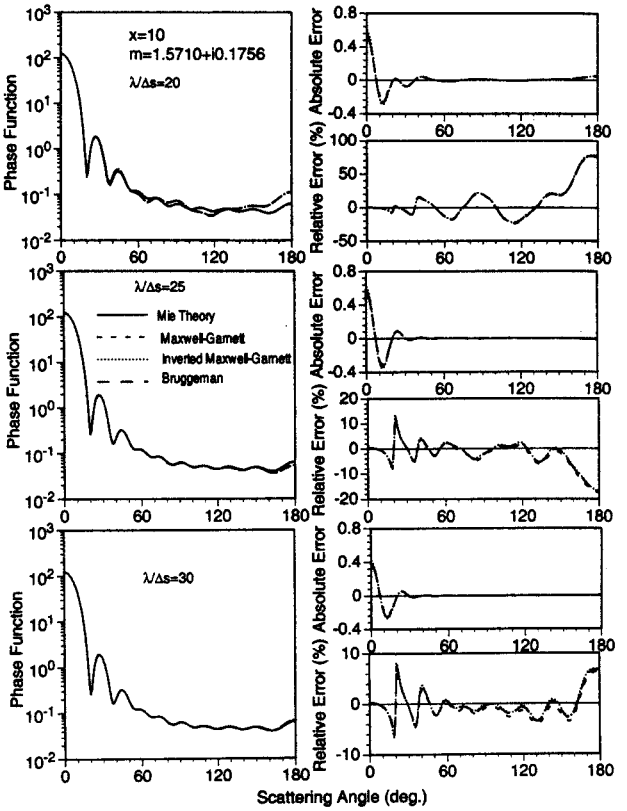

Fig. 4. Same as Fig. 3 but for a size parameter of 10.

mean permittivity. In addition, it is evident that the accuracy of the FDTD results is sensitive to the ratio of grid size to incident wavelength. The effect of grid size on the accuracy of the FDTD solution has been discussed by Yang and Liou.[3]

Figure 4 is similar to Fig. 3, except that the size parameter is now 10. For this size parameter the effect of surface roughness as a result of the staircasing approximation of the particle shape is 10 times smaller than that shown in Fig. 3 for size parameter 1. Note that the magnitude of the roughness effect is proportional to $\Delta s/r$, where r is the radius of the sphere. Thus the differences in the results obtained from the three methods applied to evaluation of the mean permittivity for the partially empty cells are negligible for a large size parameter. Parameter $\lambda/\Delta s$ is a key factor for determining the accuracy of the FDTD technique, as is evident from Fig. 3.

Table 1 lists the extinction efficiencies and single-scattering albedos associated with the phase functions for $\lambda/\Delta s = 30$ shown in Figs. 3 and 4. Comparisons of absolute and relative errors of the FDTD solution with the Mie results are listed in the table. For size parameter 1, the inaccuracy of the Maxwell-Garnett rule is approximately twice that associated with the inverted Maxwell-Garnett rule. The accuracy of the Bruggeman rule lies between those of the two other rules, as is expected from Fig. 1. For size parameter 10, the effect of staircasing is small because the roughness of the pseudosphere defined in the Cartesian grid is insignificant in comparison with the particle dimension. Again, for this size parameter, the inverted Maxwell-Garnett rule gives the best results.

To study the effect of the effective permittivity at cell edges, we have designed three schemes. In scheme 1 we apply the inverted Maxwell-Garnett rule to evaluate the mean permittivity for the partially empty cells located at the particle surface. In addition, we obtain the effective permittivity at a cell edge in the time-marching iteration of the E field by averaging the permittivity values associated with the four adjacent cells. In scheme 2, a cell is considered to be empty if 50% of its volume is outside the particle, and a unity permittivity is assigned to the cell; otherwise, the permittivity of the particle is applied to the cell. In this scheme, averaging of the permittivity is not applied to the cell edge; instead, the particle permittivity is assigned to the cell edge if any one of the adjacent cells is nonempty. If all four adjacent cells are empty, a unity permittivity is assigned to the cell edge. The procedure for constructing the particle shape in scheme 3 is the same as for scheme 2. However, in scheme 3 the averaging procedure is carried out for the cell edges on the basis of relations (11) and (12).

Figure 5 shows the phase functions computed with the these three schemes for size parameter 1 and their relative errors in comparison with the Mie re-

Table 1. Extinction Efficiencies Q_e and Single-Scattering Albedos $\tilde{\omega}$ Corresponding to the Phase Functions Shown in Figs. 3 and 4 for $\lambda/\Delta s = 30$[a]

	Q_e (FDTD)	ΔQ_e	$\Delta Q_e/Q_e$ (Mie) (%)	$\tilde{\omega}$ (FDTD)	$\Delta\tilde{\omega}$	$\Delta\tilde{\omega}/\tilde{\omega}$ (Mie) (%)
$\chi = 1$ [Q_e (Mie) = 0.7342, $\tilde{\omega}$ (Mie) = 0.3699]						
Maxwell-Garnett	0.7931	0.0589	8.02	0.3799	0.0100	2.70
Inverted Maxwell-Garnett	0.7683	0.0341	4.64	0.3757	0.0058	1.57
Bruggeman	0.7822	0.0480	6.54	0.3772	0.0073	1.97
$\chi = 10$ [Q_e (Mie) = 2.4177, $\tilde{\omega}$ (Mie) = 0.4943]						
Maxwell-Garnett	2.3904	−0.0273	−1.13	0.4987	0.0044	0.89
Inverted Maxwell-Garnett	2.3927	−0.0250	−1.03	0.4983	0.0040	0.81
Bruggeman	2.3915	−0.0262	−1.08	0.4986	0.0043	0.87

[a]Also listed are the values of absolute error and relative error for the two quantities. Note that $\Delta Q_e = Q_e$ (FDTD) − Q_e (Mie) and $\Delta\tilde{\omega} = \tilde{\omega}$(FDTD) − $\tilde{\omega}$(Mie).

sults. We selected $\lambda/\Delta s = 25$ for the computations. It is evident that scheme 2 produces the largest errors, particularly for scattering angles larger than 120°. The signs of the variations of relative error versus scattering angle are similar for schemes 2 and 3 because we used the same procedure in constructing the particle shape. However, using the averaging procedure to determine the effective permittivity for cell edges substantially improved the accuracy of the FDTD technique, as is shown by comparison of the results computed from the three schemes. We note that the relative error in forward scattering is larger in schemes 2 and 3 than in scheme 1. The magnitude of the phase function in the forward-scattering direction is approximately two times larger than in backscattering. Thus, in terms of total scattered energy, scheme 1 is also accurate.

Figure 6 is the same as Fig. 5, except that the size parameter is 10. In this case the staircasing approximation is small in comparison with the particle dimension. Thus the method of evaluating the mean dielectric constants for the partially empty cells located near the particle surface becomes less important. For this reason the errors in scheme 1 are of the same order as those in scheme 3. However, the maximum error produced by scheme 2 is approximately two times larger than those produced by schemes 1 and 3. In particular, scheme 2 produces a 40% relative error at the 20° scattering angle where a resonant minimum is shown. Evidently, the method with which the effective dielectric constant at cell edges is evaluated can substantially affect the performance of the FDTD technique. It affects mainly the locations at the interface of free space and the particle medium, regardless of the size parameter. Physically, the accuracy of the electromagnetic boundary condition (i.e., the tangential components of the E field and the normal components of the H field are continuous at medium interface) involved in the time-marching iteration of the near field in the time domain depends substantially on the correctness of the dielectric constants defined at the interface. Thus it is critical to evaluate properly the dielectric constant at the cell edges.

Table 2 lists the FDTD solutions and the associated errors for the extinction efficiencies and single-

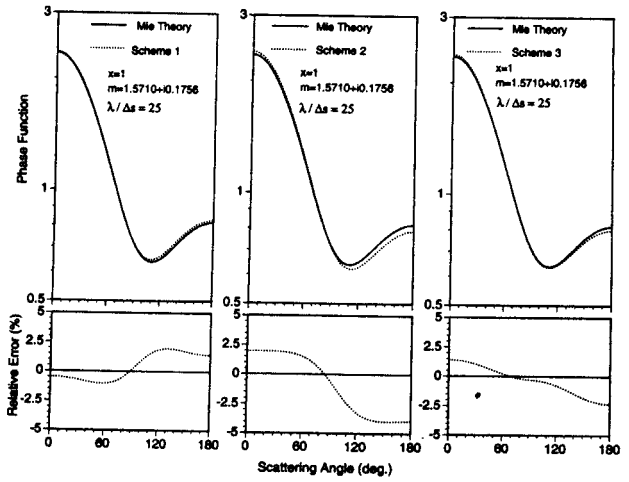

Fig. 5. Comparison of the performance of three schemes to account for the discontinuity of permittivity at the interface of free space and the particle medium in conjunction with the FDTD computation of phase function for an ice sphere with a size parameter of 1.

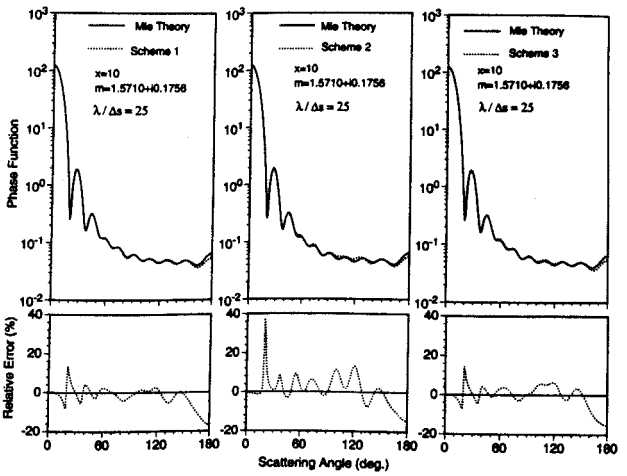

Fig. 6. Same as Fig. 5 but for a size parameter of 10.

Table 2. Extinction Efficiencies Q_e and Single-Scattering Albedos $\tilde{\omega}$ Corresponding to the Phase Functions Shown in Figs. 5 and 6[a]

Scheme Number	Q_e (FDTD)	ΔQ_e	$\Delta Q_e/Q_e$ (Mie) (%)	$\tilde{\omega}$ (FDTD)	$\Delta\tilde{\omega}$	$\Delta\tilde{\omega}/\tilde{\omega}$ (Mie) (%)
$\chi = 1$ [Q_e (Mie) = 0.7342, $\tilde{\omega}$ (Mie) = 0.3699]						
1	0.7813	0.0471	6.42	0.3814	0.0115	3.11
2	0.8526	0.1184	16.12	0.4230	0.0531	14.35
3	0.8411	0.1069	14.56	0.3945	0.0246	6.65
$\chi = 10$ [Q_e (Mie) = 2.4177, $\tilde{\omega}$(Mie) = 0.4943]						
1	2.3793	−0.0384	−1.59	0.4994	0.0051	1.03
2	2.2734	−0.1443	−5.97	0.5022	0.0079	1.60
3	2.3768	−0.0407	−1.68	0.5003	0.0060	1.20

[a]Also listed are the values of absolute error and relative error. Note that $\Delta Q_e = Q_e$ (FDTD) − Q_e (Mie) and $\Delta\tilde{\omega} = \tilde{\omega}$ (FDTD) − $\tilde{\omega}$ (Mie).

scattering albedos that correspond to the phase functions shown in Figs. 5 and 6. It is evident that substantial inaccuracies can occur if the effective permittivity values at the cell edges are not properly evaluated. The inaccuracies caused by inappropriate treatment of the permittivity at the cell edges is more significant in the computation of extinction efficiency than in the computation of the single-scattering albedo. This is so because the errors may lead to an overestimation or underestimation of the extinction and scattering cross sections in a consistent manner; thus the errors can be largely canceled in the single-scattering albedo calculations. From Figs. 5 and 6 and Table 2 it can be noted that scheme 1 is the most accurate of the three schemes. Thus we shall use scheme 1 in the rest of this study.

To demonstrate the accuracy of the present improved FDTD computational program we show in Fig. 7 the phase functions for an ice sphere at 11- and 15-μm wavelengths. The refractive indices for the two wavelengths are 1.0925 + i0.248 and 1.571 + i0.1756, respectively. Because the magnitude of the ice's refractive index at the 15-μm wavelength is approximately 1.3 times larger than that at 11 μm, the resolution of $\lambda_p/\Delta s = 25$ at the latter wavelength is equivalent to a resolution of $\lambda_p/\Delta s = 32.5$ at the former, where λ_p is the wavelength within the particle medium. For this reason we select $\lambda/\Delta s = 25$, 30, respectively, for the 11- and 15-μm wavelengths. The relative errors of the phase functions computed from the FDTD technique are less than 10%. The error maxima are noted mainly at the angular locations that correspond to the resonant minima and backscattering. Finally, it should be pointed out that the grid size must be less than 1/20 of the wavelength inside the particle to prevent substantial computational dispersion in the FDTD implementation.

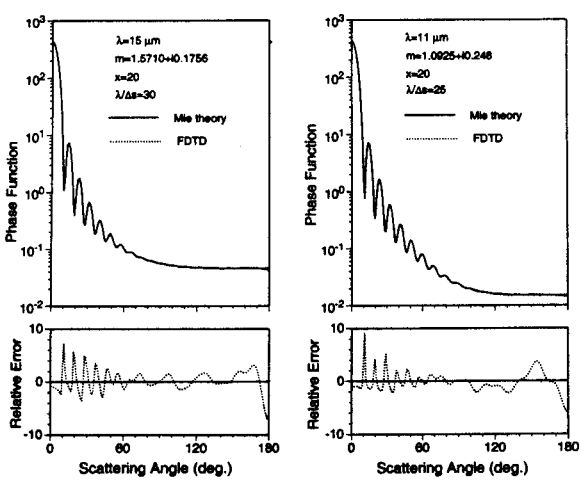

Fig. 7. Comparison of FDTD and Mie results for the phase function of ice spheres by use of grid resolutions $\lambda/\Delta s = 25$, 30, respectively, for optically thin (1.0925 + i0.248) and thick (1.5710 + i0.1756) cases.

4. Application to Light Scattering by Aerosols

The shapes of aerosols are diverse, ranging from quasi-spheres to highly irregular geometries. Mineral, dustlike, and soil aerosols are largely nonspherical particles with mean aspect ratios substantially different from unity.[13–15] Knowledge of the fundamental scattering and absorption properties of aerosols is essential to the development of a physically based and accurate retrieval algorithm for aerosol optical depth.[16] Mishchenko *et al.*[17,18] have demonstrated that the effect of nonsphericity on the optical properties of aerosols has the potential to be great and that the equivalent spherical approximation for the single-scattering properties of nonspherical particles based on Mie theory is physically inappropriate and often misleading. Using a mixture of prolate and oblate spheroids for aerosols, Mishchenko *et al.*[17] showed that the errors that are due to neglect of particle nonsphericity are much larger than those that stem from measurement errors and can easily exceed 100% in the retrieval of aerosol optical depth. In what follows, we investigate the deviation of the phase functions computed for convex and concave aerosols based on the FDTD technique from those computed for spheres and spheroids.

The sizes of convex and concave aerosols can be specified in terms of their peripheral spheroids. To construct a convex geometry, for example, a ten-faced convex shape, we select seven points on a sphere with a unit radius. The coordinate values of these seven points can be given by $(\tilde{x}_i, \tilde{y}_i, \tilde{z}_i) = (\sin\theta_i \cos\varphi_i, \sin\theta_i \sin\varphi_i, \cos\theta_i)$, where $i = 1$–7 indicate the seven

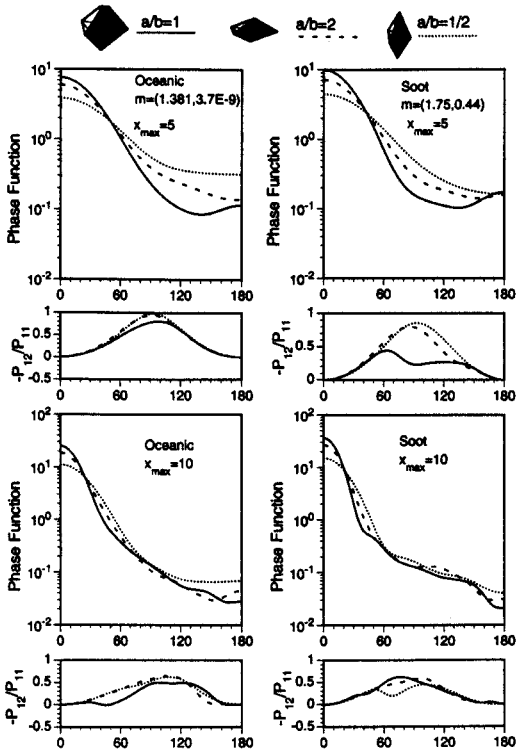

Fig. 8. Comparison of phase function and degree of linear polarization for randomly oriented six-faced convex aerosol particles with aspect ratios of 1, 2, and 1/2.

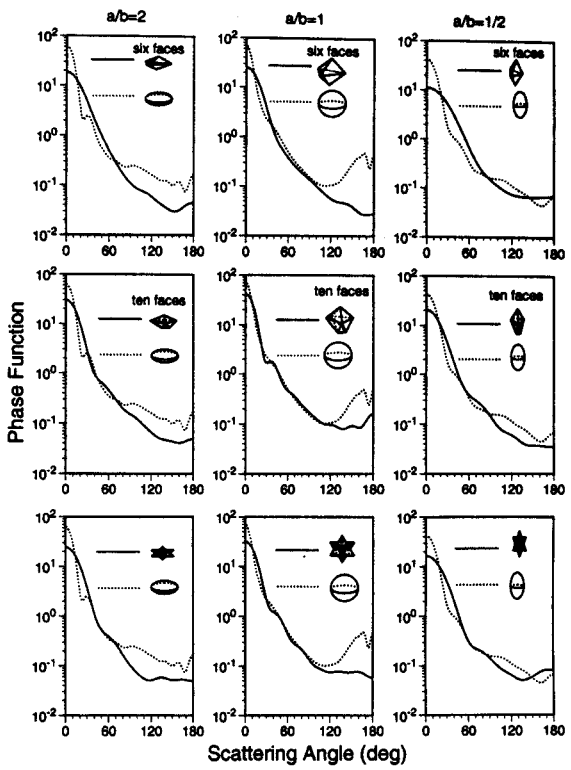

Fig. 9. Comparison of the phase functions for oceanic aerosol particles of various shapes. For spherical particles, i.e., $a/b = 1$, a power-law size distribution is employed to smooth out the resonant fluctuations. The size parameter used is $x_{max} = 10$.

points and θ_i and φ_i are the zenith and azimuthal angles of the points, respectively. One can construct a ten-faced convex shape that is enveloped by a unit sphere by properly connecting the seven points. To obtain a convex shape with a desired size and aspect ratio, we can stretch the coordinate values, using the relationship $(x_i, y_i, z_i) = (a\tilde{x}_i, a\tilde{y}_i, b\tilde{z}_i)$, where a and b are the semiaxes of the spheroid that envelops the convex particle. We obtain an oblate particle if $a > b$ and a prolate particle if $a < b$.

To construct a concave particle we select two right-triangular pyramids. The base of one of the pyramids faces up, and that of the other pyramid faces down. In addition, the distance from the apexes to the centers of the pyramids is selected to be unity. The two pyramids share the same origin. Thus the apexes of the two pyramids are confined on a unit sphere. Employing the preceding coordinate stretching procedure, we can obtain various aspect ratios and sizes for the concave geometry.

We select two refractive indices, $m = 1.38 + i3.9 \times 10^{-9}$ and $1.75 + i0.44$, which represent aerosols with oceanic sources and soots, respectively. Figure 8 shows the phase functions and the degrees of linear polarization computed for various six-faced convex aerosols with aspect ratios $a/b = 1/2$, 1, 2. The particles are assumed to be randomly oriented in space. For a size parameter of 5, substantial differences are noted for the three aspect ratios in the side-scattering directions about 120°. For a size parameter of 10, the differences in the phase function are mainly in forward scattering. The volume associated with $a/b = 1$ is larger than those for $a/b = 1/2$, 2. Thus the particles with $a/b = 1$ have a larger scattering capability and produce a stronger forward peak. However, the particle volume seems not to be a dominant factor in determining the scattering properties. For example, the phase functions for $a/b = 1/2$, 2 are quite different, although the corresponding particle volume is similar in these two cases. The pattern of degrees of linear polarization is not sensitive to the aspect ratio, except for a size parameter of 5 with strong absorption.

Figure 9 shows the phase functions for convex and concave aerosols for three aspect ratios in comparison with those for spheroids that have the same aspect ratios. The scattering properties of spheroidal particles were computed by the T-matrix method.[19] For $a/b = 1$, the phase functions for nonspherical particles are substantially smaller than those for spheres in the scattering angular region 120°–180°; in particular, the differences in the results for spherical and nonspherical particles are pronounced in the backscattering. For $a/b = 2, 1/2$, we also see substantial differences between smooth spheroids and irregular convex and concave particles.

Finally, we compare theoretical phase function results with experimental data, as shown in Fig. 10. The theoretical results correspond to an ensemble of randomly oriented concave and convex particles. The experimental data are determined from the

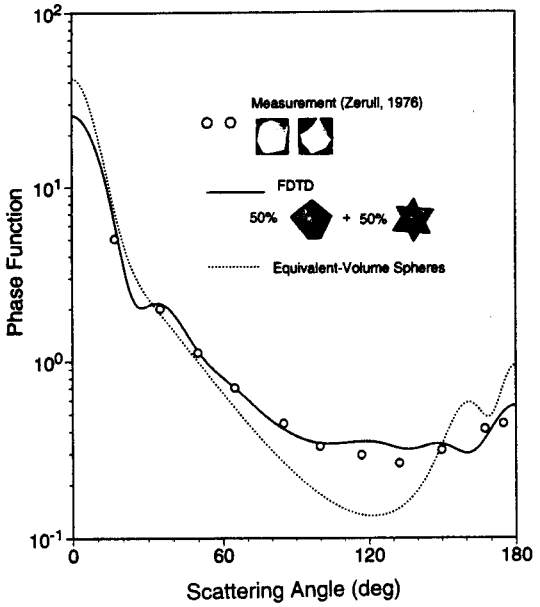

Fig. 10. Phase functions measured by the microwave analog technique and computed from the FDTD method for randomly oriented convex and concave particles with a refractive index $m = (1.5 + i0.005)$ and size parameters ranging from 5.9 to 17.8.

measurements made by Zurell,[20] who used the microwave analog technique for randomly oriented convex and concave particles with a refractive index $m = 1.5 + i0.005$ and size parameters ranging from 5.9 to 17.8. The data have been reanalyzed by Pollack and Cuzzi.[21] The equivalent spherical results are based on the volume of the particle geometry used in the theoretical computation. The phase function for nonspherical particles computed for the FDTD method appears to match the experimental results.

5. Conclusions

We have improved the Cartesian FDTD scheme by properly evaluating the dielectric constant for partially empty cells and the cell edges located at the interface of free space and the particle medium. We have also increased the efficiency of the FDTD program by employing the PML technique and coding in FORTRAN90.

Based on the improved FDTD program, the accuracy of various approaches to dealing with the subgrid variation and discontinuity of a dielectric constant at the particle surface was investigated. The magnitude of the staircasing approximation of particle shape on a Cartesian grid is inversely proportional to the ratio of the grid size to the particle dimension. For a small size parameter, the staircasing effect is substantially large. We have illustrated that the inverted Maxwell-Garnett rule is the most effective in reducing the staircasing effect. With an increase in the size parameter, the staircasing effect decreases, and the method that one uses to evaluate the mean permittivity becomes less important. We also investigated the effect of the discontinuity of permittivity at the interface of free space and the particle medium that exists regardless of the pseudoparticle shape defined in the Cartesian grid. This effect must be properly accounted for because the electromagnetic boundary condition implied in the computation of the near field essentially depends on the permittivity at the surface cell edges. Numerical results have revealed that the effective permittivity given by the average of the permittivity values of four adjacent cells can substantially reduce the discontinuity effect.

We applied the improved FDTD code to the study of light scattering by nonspherical aerosols. We constructed convex and concave particle shapes to resemble dust and some irregular aerosols and carried out calculations of phase function and linear polarization patterns. Comparisons with results computed from the T matrix for spheroids and the Mie theory for spheres were made. We showed that substantial differences occur, particularly in backscattering directions. Finally, we found that the theoretical phase function computed for the convex and concave particles is in reasonably good agreement with available microwave analog experimental results.

This research has been supported by National Science Foundation grant ATM-97-96277 and NASA grant 5-7738 and partially by the U.S. Office of Naval Research.

References

1. S. K. Yee, "Numerical solution of initial boundary value problems involving Maxwell's equation in isotropic media," IEEE Trans. Antennas Propag. **AP-14,** 302–307 (1966).
2. P. Yang and K. N. Liou, "Light scattering by hexagonal ice crystals: comparison of finite-difference time domain and geometric optics models," J. Opt. Soc. Am. A **12,** 162–176 (1995).
3. P. Yang and K. N. Liou, "Finite-difference time domain method for light scattering by small ice crystals in three-dimensional space," J. Opt. Soc. Am. A **13,** 2072–2085 (1996).
4. J. C. Maxwell-Garnett, "Colours in metal glasses and in metallic films," Philos. Trans. R. Soc. A **203,** 385–420 (1904).
5. B. J. Berenger, "A perfectly matched layer for the absorption of electromagnetic waves," J. Comput. Phys. **114,** 185–200 (1994).
6. B. J. Berenger, "Three-dimensional perfect matched layer for the absorption of electromagnetic wave," J. Comput. Phys. **127,** 363–379 (1996).
7. C. A. G. Bruggeman, "Gerechung verschiedener physikalischer Konstanten von heterogenen Subsganzen," Ann. Phys. (Leipzig) **24,** 636–679 (1935).
8. P. Yang and K. N. Liou, "An efficient algorithm for truncating spatial domain in modeling light scattering by finite-difference technique," J. Comput. Phys. **140,** 346–369 (1998).
9. D. S. Katz, E. T. Thiele, and A. Taflove, "Validation and extension to three dimensions of Berenger PML absorbing boundary condition for FD-TD meshes," IEEE Microwave Guided Wave Lett. **4,** 268–270 (1994).
10. W. Sun, Q. Fu, and Z. Chen, "Finite-difference time-domain solution of light scattering by dielectric particles with a perfectly matched layer absorbing boundary condition," Appl. Opt. **38,** 3141–3151 (1999).
11. P. Yang and K. N. Liou, "Finite difference time domain method

for light scattering by nonspherical and inhomogeneous particles," in *Light Scattering by Nonspherical Particles: Theory, Measurements, and Applications*, M. I. Mishchenko, J. W. Hovenier, and L. D. Travis, eds. (Academic, San Diego, Calif., 1999), pp. 173–221.
12. G. Lazzi and O. P. Gandhi, "On the optimal design of the PML absorbing boundary condition for the FDTD code," IEEE Trans. Antennas Propag. **45,** 914–916 (1996).
13. S. C. Hill, A. C. Hill, and P. W. Barber, "Light scattering by size/shape distribution of soil particles and spheroids," Appl. Opt. **23,** 1025–2430 (1988).
14. K. Okada, A. Kobayashi, Y. Iwasaka, H. Naruse, T. Tanaka, and O. Nemoto, "Features of individual Asian dust-storm particles collected at Nagoya, Japan," J. Meteorol. Soc. Jpn. **65,** 515–521 (1987).
15. T. Nakajima, M. Tanaka, M. Yamano, M. Shiobara, K. Arao, and Y. Nakanishi, "Aerosol optical characteristics in the yellow sand events observed in May 1982 at Nagasaki. II. Models," J. Meteorol. Soc. Jpn. **67,** 279–291 (1989).
16. M. Wang and H. R. Gordan, "Estimating aerosol optical properties over the oceans with multiangle imaging spectroradiometer: some preliminary results," Appl. Opt. **33,** 4042–4057 (1994).
17. M. I. Mishchenko, A. A. Lacis, B. E. Carlson, and L. D. Travis, "Nonsphericity of dust-like tropospherical aerosols: implications for aerosol remote sensing and climate modeling," Geophys. Res. Lett. **22,** 1077–1080 (1995).
18. M. I. Mishchenko, L. D. Travis, R. A. Kahn, and R. A. West, "Modeling phase functions for dustlike tropospheric aerosols using a shape mixture of randomly oriented polydisperse spheroids," J. Geophys. Res. **102,** 16,831–16,847 (1997).
19. M. I. Mishchenko and L. D. Travis, "Light scattering by polydispersions of randomly oriented spheroids with sizes comparable to wavelengths of observation," Appl. Opt. **33,** 7206–7225 (1994).
20. R. H. Zerull, "Scattering measurements of dielectric and absorbing nonspherical particles," Beitr. Phys. Atmos. **49,** 168–188 (1976).
21. J. B. Pollack and J. N. Cuzzi, "Scattering by nonspherical particles of size comparable to a wavelength: a new semi-empirical theory and its application to tropospheric aerosols," J. Atmos. Sci. **37,** 868–881 (1980).